

Cite this: *Dalton Trans.*, 2020, **49**,  
659

## Photoelectrochemical water-splitting over a surface modified p-type Cr<sub>2</sub>O<sub>3</sub> photocathode†

Keita Sekizawa,<sup>id</sup>\* Keiichiro Oh-ishi<sup>id</sup> and Takeshi Morikawa<sup>id</sup>

Cr<sub>2</sub>O<sub>3</sub> is a p-type semiconductor with a negative conduction band minimum position suitable for photo-cathodic H<sub>2</sub> generation. Therefore, Cr<sub>2</sub>O<sub>3</sub> is a candidate photocathode material for photoelectrochemical (PEC) water-splitting. However, Cr<sub>2</sub>O<sub>3</sub> has not yet been applied for the purpose of H<sub>2</sub> generation because the efficiency and stability of the photocurrent generated by a Cr<sub>2</sub>O<sub>3</sub> electrode are poor, due to high defect and vacancy concentrations. In the present work, the Cr<sub>2</sub>O<sub>3</sub> surface was modified with n-type TiO<sub>2</sub> after which Pt particles were deposited to catalyse H<sub>2</sub> production. The TiO<sub>2</sub> overlayer passivated the Cr<sub>2</sub>O<sub>3</sub> surface states that otherwise cause deleterious interactions with the Pt particles. This layer also improved charge separation from the conduction band of Cr<sub>2</sub>O<sub>3</sub> to the Pt co-catalyst, by forming a p–n junction. As a result of the TiO<sub>2</sub> insertion, the cathodic photocurrent resulting from light absorption by Cr<sub>2</sub>O<sub>3</sub> was enhanced and stabilized. This represents the first-ever use of Cr<sub>2</sub>O<sub>3</sub> as a light-absorbing material in a multi-layered electrode to accomplish PEC water-splitting for H<sub>2</sub> generation.

Received 6th November 2019,  
Accepted 28th November 2019

DOI: 10.1039/c9dt04296b

rsc.li/dalton

### Introduction

H<sub>2</sub> has attracted considerable interest as a clean energy carrier that does not produce CO<sub>2</sub>, and is expected to play an important role in meeting growing worldwide energy requirements.<sup>1–3</sup> Photoelectrochemical (PEC) water-splitting into H<sub>2</sub> and O<sub>2</sub> using semiconductor electrodes is a promising approach to the direct conversion of solar energy into H<sub>2</sub>.<sup>4–6</sup> In 1972, Honda and Fujishima first reported the PEC decomposition of water to H<sub>2</sub>, utilizing an n-type TiO<sub>2</sub> electrode in conjunction with UV illumination and the application of an external electrical bias.<sup>7</sup> After this pioneering work, numerous semiconductor photocatalysts and photoelectrodes were developed.<sup>8–17</sup> It is widely recognized that most semiconductors require the addition of a sacrificial electron donor or the application of an external voltage, as the edges of the conduction band and valence band typically do not straddle the water reduction and oxidation potentials. As a means of promoting water splitting without an external electrical bias while separately generating H<sub>2</sub> and O<sub>2</sub> at different electrodes, PEC devices containing electrically connected p-type and n-type semiconductor photoelectrodes have been designed.<sup>18–22</sup> Metal oxides are suitable semiconductor materials because they are abundant and relatively in-

expensive. Since metal oxide semiconductors predominantly exhibit n-type characteristics, because they readily form oxygen vacancies, there have been many reports regarding the use of n-type semiconductor photoanodes to generate oxygen. In contrast, there are only a few native p-type semiconductor oxides, because the cation vacancies or oxygen interstitials that produce p-type conductivity are not easily generated.<sup>23,24</sup> Moreover, utilizing photocathodes for H<sub>2</sub> evolution requires that the conduction band minimum of the cathode material be more negative than the H<sup>+</sup>/H<sub>2</sub> reduction potential (0 V vs. reversible hydrogen electrode; RHE). The oxide p-type semiconductors meeting this requirement are limited, with examples being copper oxides<sup>25,26</sup> and iron oxides.<sup>27–29</sup>

Cr<sub>2</sub>O<sub>3</sub> is one of the few oxides exhibiting p-type conductivity.<sup>30,31</sup> Standard Cr<sub>2</sub>O<sub>3</sub> has a hexagonal corundum structure.<sup>32,33</sup> In the unit cell of non-defective Cr<sub>2</sub>O<sub>3</sub>, two-thirds of the octahedral oxygen sites are occupied by Cr while the remaining one-third are unoccupied (Fig. S1†). Consequently, removing Cr atoms from the cell generates vacancies. Moreover, the migration of Cr to the pre-existing empty sites (typically interstitial sites in nearby locations) results in Cr Frenkel defects, while the diffusion of O atoms generates O vacancies. These defects and vacancies are known to determine the appearance of p-type and n-type characteristics.<sup>34–38</sup> The defect formation energy values calculated using first-principles DFT+U by Diawara *et al.*<sup>38</sup> suggest that the stability of defects follows the order: Cr Frenkel defect > Cr vacancy > O vacancy. Therefore, native Cr<sub>2</sub>O<sub>3</sub> tends to form metal-deficient sites that result in p-type conductivity. The p-type conductivity of Cr<sub>2</sub>O<sub>3</sub> has been applied to produce

Toyota Central R&D Laboratories, Inc., 41-1, Yokomichi, Nagakute, Aichi 480-1192, Japan. E-mail: sekizawa@mosk.tytlabs.co.jp

† Electronic supplementary information (ESI) available: An image of the crystal structure, UV/visible absorption spectra, STEM-EDX images and PEC properties. See DOI: 10.1039/C9DT04296B



hole transfer layers inserted between a back contact and a semiconductor photoabsorber, such as  $\text{CuO}$ <sup>26</sup> or  $\text{Fe}_2\text{O}_3$ .<sup>39</sup> Moreover, the conduction band minimum of  $\text{Cr}_2\text{O}_3$  is located at a much more negative level than the redox potential for water reduction.<sup>40,41</sup> Even so, to the best of our knowledge, there have been no reports of the application of  $\text{Cr}_2\text{O}_3$  as a photoabsorber in photocathodes for  $\text{H}_2$  generation. This may be due to the ready formation of various defects and vacancies in  $\text{Cr}_2\text{O}_3$ . Defects, vacancies and surface dangling bonds form states within the bandgap that can serve as recombination centres for photogenerated charges (Scheme 1a). In addition, a high density of bandgap states will transition  $\text{Cr}_2\text{O}_3$  into a conductor.<sup>42,43</sup> However, if photogenerated charges can be prevented from transferring to such bandgap states, it may be possible to apply  $\text{Cr}_2\text{O}_3$  as a photocathode for  $\text{H}_2$  evolution. Furthermore, since band gap narrowing *via* doping with specific ions has already been realized,<sup>44–47</sup>  $\text{Cr}_2\text{O}_3$  also has the potential to become a visible-light responsive photocathode.

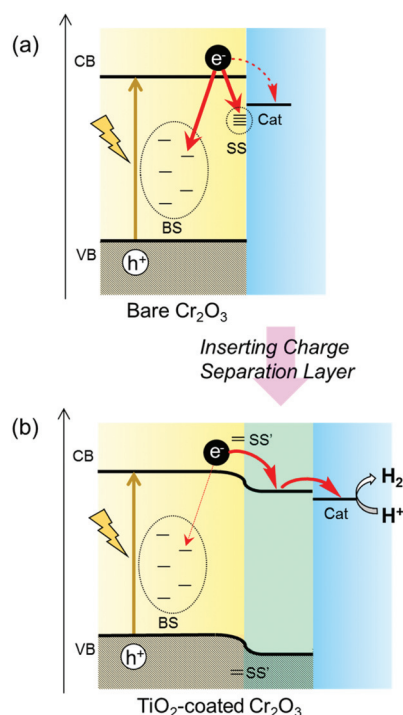
Recently, it has been reported that various benefits can be obtained by the surface treatment of photoelectrodes.<sup>48,49</sup> Specifically, such processing can protect the unstable surface of the photoabsorber from photocorrosion by preventing contact with the electrolyte. Furthermore, this treatment can passivate surface states. When the atomic orbitals of surface states couple with those of deposits, the coupled surface states can be moved away from the band gap because of the for-

mation of bonding and antibonding states<sup>49</sup> (shown as  $\text{SS}'$  in Scheme 1b). Moreover, the formation of a heterojunction by surface treatment is expected to modify band bending due to the diffusion of charge carriers between two semiconductors having different Fermi levels. This modification should enhance both photogenerated electron–hole separation and carrier transfer. Therefore, in the present work, the  $\text{Cr}_2\text{O}_3$  surface was modified with n-type  $\text{TiO}_2$  to ensure both charge separation and passivation. Subsequently, Pt particles were deposited on the  $\text{TiO}_2$  layer to catalyse  $\text{H}_2$  production<sup>50</sup> (Scheme 1b).

## Results and discussion

### Structural and optical properties of $\text{Cr}_2\text{O}_3$

$\text{Cr}_2\text{O}_3$  electrodes were prepared by the radio frequency (RF) reactive magnetron sputtering of Cr targets in an  $\text{Ar}/\text{O}_2$  (9 : 1) plasma to give a thickness of 60 nm on a transparent conductive oxide (TCO;  $\text{SnO}_2$ -coated indium tin oxide (ITO)), followed by annealing at 823 K. As shown in Fig. 1 (blue line), the X-ray diffraction (XRD) patterns of the resulting  $\text{Cr}_2\text{O}_3$  on TCO exhibit peaks at  $33.8^\circ$ ,  $36.4^\circ$  and  $55.3^\circ$ , which are assignable to the (104), (110) and (116) diffractions of  $\text{Cr}_2\text{O}_3$  (eskolaite), respectively. All other peaks are attributed to  $\text{SnO}_2$  or ITO, while there are no peaks due to impurities. The X-ray photoelectron spectroscopy (XPS) data obtained from the resulting  $\text{Cr}_2\text{O}_3$  layer are presented in Fig. 2a, and are similar to those produced by the reference  $\text{Cr}_2\text{O}_3$  (Fig. 2c). The peaks at binding energies of 576.5 and 586.1 eV are ascribed to the Cr  $2p_{3/2}$  and  $2p_{1/2}$  signals of Cr(III) oxide, respectively. Although the Cr  $2p_{3/2}$  peak includes a shoulder, this peak shape is typical of  $\text{Cr}_2\text{O}_3$  and is attributed to the multiplet structure of Cr(III) oxide.<sup>51</sup> Pt was subsequently deposited on the electrodes as a co-catalyst for  $\text{H}_2$  evolution from water by sputtering, to a nominal thickness of 1 nm. Scanning transmission electron microscopy (STEM) combined with energy-dispersive X-ray spectroscopy (EDX) for elemental mapping was used to assess cross-sections of the Pt/ $\text{Cr}_2\text{O}_3$  sample, as shown in Fig. 3a. In



**Scheme 1** Schematic diagram of the expected electron transfer process in (a) bare  $\text{Cr}_2\text{O}_3$  and (b)  $\text{TiO}_2$ -coated  $\text{Cr}_2\text{O}_3$  photocathodes. BS and SS indicate bulk states and surface states, respectively. The former are generated by defects and vacancies, while the latter result from surface dangling bonds.

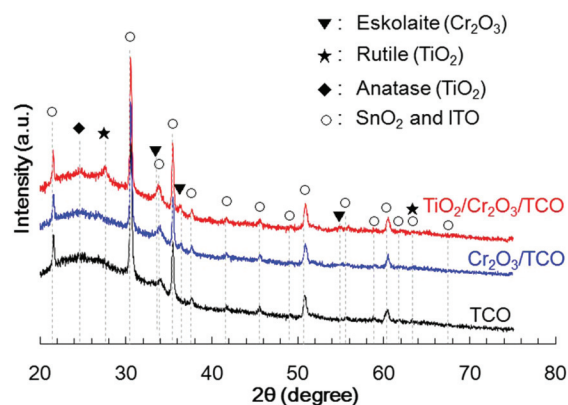


**Fig. 1** XRD patterns obtained from TCO (black line),  $\text{Cr}_2\text{O}_3$ /TCO (blue line) and  $\text{TiO}_2$ / $\text{Cr}_2\text{O}_3$ /TCO (red line).





Fig. 2 XPS spectra obtained from a Cr<sub>2</sub>O<sub>3</sub> electrode (a) before and (b) after photoelectrolysis for 1 h and from (c) the reference Cr<sub>2</sub>O<sub>3</sub>.

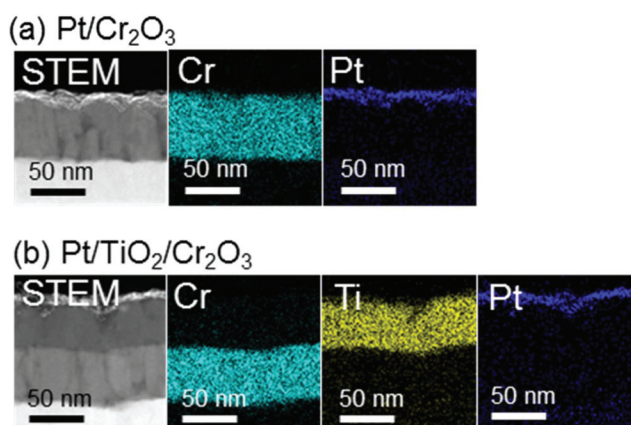


Fig. 3 Cross-sectional STEM images and STEM-EDX elemental maps for (a) Pt/Cr<sub>2</sub>O<sub>3</sub> and (b) Pt/TiO<sub>2</sub>/Cr<sub>2</sub>O<sub>3</sub>.

both electrodes, a flat Cr<sub>2</sub>O<sub>3</sub> layer was observed on the TCO film.

UV/visible absorption spectra were acquired by a transmission method for this electrode and are shown in Fig. 4 as a blue line. Although an interference spectrum was included in the original spectrum, the absorption edge is evident at 410 nm, in agreement with a Cr<sub>2</sub>O<sub>3</sub> reference bulk powder (Fig. S2†) and previous reports<sup>52–54</sup>

### PEC properties of the Cr<sub>2</sub>O<sub>3</sub> electrodes

Fig. 5a and b present the current–potential curves obtained from the Cr<sub>2</sub>O<sub>3</sub>-based electrodes and from a TiO<sub>2</sub> electrode in a 0.5 M Na<sub>2</sub>CO<sub>3</sub>:NaHCO<sub>3</sub> (1:1) buffer electrolyte (pH 9.7) under chopped AM 1.5 irradiation (1 Sun; 100 mW cm<sup>-2</sup>), with irradiation of the deposited semiconductor side. The bare Cr<sub>2</sub>O<sub>3</sub> electrode (Fig. 5a, black line) generated a cathodic photocurrent in the negative voltage range below +1.1 V vs. RHE, although it also produced a dark current. The photocurrent density of this sample at +0.1 V, after removing the dark current density from the current density produced during light irradiation, was  $-15 \mu\text{A cm}^{-2}$ . This cathodic photocurrent indicates that the Cr<sub>2</sub>O<sub>3</sub> electrode exhibited p-type conductivity



Fig. 4 UV/visible absorption spectra for TiO<sub>2</sub>/Cr<sub>2</sub>O<sub>3</sub> (red line), Cr<sub>2</sub>O<sub>3</sub> (blue line) and TiO<sub>2</sub> (black line) on TCO and the sum of the Cr<sub>2</sub>O<sub>3</sub> and TiO<sub>2</sub> spectra (green line). E<sub>g</sub> indicates the absorption edges for the band-gap excitation.

and could possibly be utilized as a photocathode for water splitting. However, a large cathodic dark current was apparent between +1.1 and +1.5 V, including a peak of  $-240 \mu\text{A cm}^{-2}$  at +1.08 V. This significant dark current indicates that electrons leaked to defect states and surface states in the band gap. Upon applying a constant potential of +0.11 V vs. RHE, the dark current was decreased due to electron charging, while the cathodic photocurrent was observed to decay from 8.1 to  $0.9 \mu\text{A cm}^{-2}$  during 1 sun irradiation for 3 min (Fig. 5c, black line). After 1 h of photoelectrolysis, the dark current was slightly increased but the difference in the photocurrent in the current–potential curve was negligible (Fig. S3†). In addition, when the chemical state of the Cr<sub>2</sub>O<sub>3</sub> surface was examined by XPS, there were almost no differences before and after the photoelectrolysis (Fig. 2a and b, respectively), suggesting no self-reduction of Cr<sub>2</sub>O<sub>3</sub> by the photogenerated electrons. Therefore, Cr<sub>2</sub>O<sub>3</sub> itself was stable during photoelectrolysis but photoelectrons could be trapped in defects and surface states, resulting in photocurrent decay.

Pt was deposited on Cr<sub>2</sub>O<sub>3</sub> as a co-catalyst for H<sub>2</sub> evolution, by sputtering. The current–potential curve produced by the resulting Pt/Cr<sub>2</sub>O<sub>3</sub> exhibited a new and significant dark current between 0.5 and 0.9 V, including a peak of  $-700 \mu\text{A cm}^{-2}$  at +0.63 V. Moreover, the photocurrent was negligible after Pt loading (Fig. 5a, green line). Although the dark current was reduced by applying a constant potential of +0.11 V vs. RHE under dark conditions, the photocurrent was smaller than that obtained from pure Cr<sub>2</sub>O<sub>3</sub> (Fig. 5c, green line). The large dark current in the current–potential curve suggests that new band-gap states were generated within the bandgap of Cr<sub>2</sub>O<sub>3</sub> following Pt deposition. The appearance of these deleterious band gap states can possibly be ascribed to the coupling of the atomic orbitals of dangling atoms at the Cr<sub>2</sub>O<sub>3</sub> surface with those of deposited Pt atoms. The resulting bonding and anti-bonding orbitals would generate deleterious band-gap states,<sup>55</sup> leading to electron leakage and recombination of photo-gener-





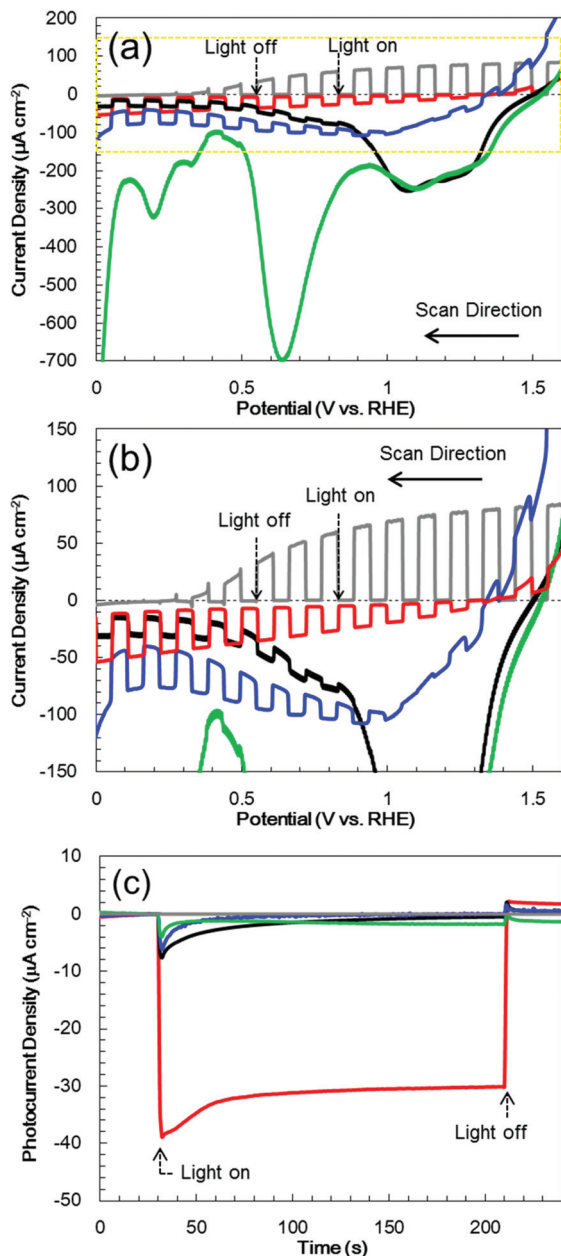


**Fig. 5** (a) Photocurrent–potential characteristics under chopped light irradiation, (b) enlargement of the area in the yellow dotted line in (a), and (c) photocurrent transients at +0.11 V vs. RHE in a 0.5 M  $\text{Na}_2\text{CO}_3:\text{NaHCO}_3$  (1:1) buffer electrolyte (pH 9.7) under one sun ( $100 \text{ mW cm}^{-2}$ , AM 1.5) illumination for the bare  $\text{Cr}_2\text{O}_3$  (black line), Pt/ $\text{Cr}_2\text{O}_3$  (green line),  $\text{TiO}_2$  (grey line),  $\text{TiO}_2/\text{Cr}_2\text{O}_3$  (blue line) and Pt/ $\text{TiO}_2/\text{Cr}_2\text{O}_3$  (red line).

ated electrons and holes. As a result, the addition of Pt nanoparticles to the  $\text{Cr}_2\text{O}_3$  surface diminished the photocurrent without acting as a co-catalyst for  $\text{H}_2$  evolution.

#### Coating with $\text{TiO}_2$ as passivation and charge-separation layer

$\text{TiO}_2$  overlayers with thicknesses ranging from 10 to 120 nm were subsequently deposited by sputtering a  $\text{TiO}_2$  target in an  $\text{Ar}/\text{O}_2$  (4:1) plasma onto  $\text{Cr}_2\text{O}_3$ . This was followed by post-

annealing at 748 K. The XRD patterns generated by  $\text{TiO}_2/\text{Cr}_2\text{O}_3/\text{TCO}$  (Fig. 1, red line) exhibit peaks attributable to anatase (101), and rutile (110) and (310) diffractions at  $24.8^\circ$ ,  $27.8^\circ$  and  $63.4^\circ$ , respectively. In the STEM-EDX images for the Pt/ $\text{TiO}_2/\text{Cr}_2\text{O}_3$  electrode (Fig. 3b), the  $\text{TiO}_2$  layer completely covered the  $\text{Cr}_2\text{O}_3$  surface, preventing contact with both the Pt and the electrolyte. The UV/visible absorption spectrum of the  $\text{TiO}_2/\text{Cr}_2\text{O}_3$  electrode was essentially consistent with the sum of the spectra of the  $\text{TiO}_2$  and  $\text{Cr}_2\text{O}_3$  electrodes (Fig. 4, grey dotted line). The absorption edge of the  $\text{TiO}_2$  electrode (Fig. 4, black line) was observed at 380 nm, consistent with a  $\text{TiO}_2$  reference bulk powder (Fig. S2†) and the previous report.<sup>56</sup> These data indicate that simulated solar radiation imparted to the  $\text{TiO}_2$  side should be absorbed by both  $\text{TiO}_2$  and  $\text{Cr}_2\text{O}_3$ .

In photocurrent-potential curves, the surface of  $\text{Cr}_2\text{O}_3$  was subsequently coated with a 60 nm thick  $\text{TiO}_2$  layer. The resulting  $\text{TiO}_2/\text{Cr}_2\text{O}_3$  photocathode generated a cathodic photocurrent below +1.1 V (Fig. 5b, blue line). The photocurrent at +0.1 V was  $-35 \mu\text{A cm}^{-2}$ , and so exceeded that obtained from the bare  $\text{Cr}_2\text{O}_3$  ( $-15 \mu\text{A cm}^{-2}$ ). Although the  $\text{TiO}_2$  electrode (without  $\text{Cr}_2\text{O}_3$ ) exhibited an anodic photocurrent at values more positive than +0.3 V (Fig. 5b, grey line), the photocurrent of  $\text{TiO}_2/\text{Cr}_2\text{O}_3$  cannot be explained as a combination of those for  $\text{TiO}_2$  and  $\text{Cr}_2\text{O}_3$ . The cathodic photocurrent produced by  $\text{TiO}_2/\text{Cr}_2\text{O}_3$  was also larger than that for  $\text{Cr}_2\text{O}_3$ . The anodic photocurrent produced by  $\text{TiO}_2/\text{Cr}_2\text{O}_3$  was smaller and appeared at a more positive potential than that for  $\text{TiO}_2$ . This positive shift of the onset potential for the anodic photocurrent can be explained by the formation of a p–n junction. The Fermi level of the n-type  $\text{TiO}_2$  would be expected to be shifted positively following the formation of a junction with the p-type  $\text{Cr}_2\text{O}_3$  because the Fermi levels of  $\text{TiO}_2$  and  $\text{Cr}_2\text{O}_3$  would be equalized by carrier diffusion. Moreover, the  $\text{Cr}_2\text{O}_3$  layer would be expected to inhibit photogenerated electron transfer from  $\text{TiO}_2$  to TCO, because the conduction band minimum of  $\text{Cr}_2\text{O}_3$  is higher than that of  $\text{TiO}_2$ . Hence,  $\text{TiO}_2/\text{Cr}_2\text{O}_3$  generated a cathodic photocurrent. Moreover, the dark current produced by  $\text{TiO}_2/\text{Cr}_2\text{O}_3$  decreased, from  $-240$  to  $-100 \mu\text{A cm}^{-2}$ , by the  $\text{TiO}_2$  coating, indicating a decrease in the electron transfer to the band-gap states. Since the recombination of photo-generated electrons and holes at the band-gap states was suppressed, the photocurrent was enhanced by the  $\text{TiO}_2$  coating. However, at a constant potential of +0.11 V vs. RHE, the photocurrent also decayed after irradiation (Fig. 5c, blue line).

Following the above trials, Pt nanoparticles were deposited on  $\text{TiO}_2/\text{Cr}_2\text{O}_3$  as a co-catalyst. The resulting Pt/ $\text{TiO}_2/\text{Cr}_2\text{O}_3$  specimen exhibited a cathodic photocurrent below +1.4 V (Fig. 5b, red line), with an onset potential more positive than that of  $\text{TiO}_2/\text{Cr}_2\text{O}_3$ . In addition, the dark current was diminished by the Pt loading. At a constant potential of +0.11 V vs. RHE, the cathodic photocurrent was larger and more stable than those of the other electrodes (Fig. 5c, red line). Thus, in contrast to the results obtained from the direct deposition of Pt on  $\text{Cr}_2\text{O}_3$  (Fig. 5a, green and black lines), there was no decrease in the photocurrent and an increase in the dark current. These results demonstrate that the  $\text{TiO}_2$  overlayer pas-



sivated the  $\text{Cr}_2\text{O}_3$  surface states to prevent the generation of new band-gap states *via* the coupling of  $\text{Cr}_2\text{O}_3$  and Pt. As a result, the dark current due to electron leakage to band-gap states was decreased. The photocurrent was also enhanced, because the photoelectrons generated in  $\text{Cr}_2\text{O}_3$  were able to flow to the Pt nanoparticles *via* the  $\text{TiO}_2$  layer, after which they were consumed for  $\text{H}_2$  evolution.

### Effect of the $\text{TiO}_2$ overlayer thickness

In order to optimize the thickness of the  $\text{TiO}_2$  layer on the  $\text{Cr}_2\text{O}_3$  electrode, Pt/ $\text{TiO}_2$ / $\text{Cr}_2\text{O}_3$  electrodes having  $\text{TiO}_2$  thicknesses of 10, 30, 60, 80 and 120 nm were prepared by adjusting the deposition time in the  $\text{TiO}_2$  sputtering. UV/visible absorption spectra acquired by a transmission method for these electrodes are shown in Fig. S4.† It can be seen that the absorptions in  $\lambda < 380$  nm increase in proportion to the thickness of  $\text{TiO}_2$  because the absorption edge of  $\text{TiO}_2$  is 380 nm (Fig. 4). The photocurrent transients of these specimens were assessed under irradiation with simulated solar radiation ( $100 \text{ mW cm}^{-2}$ , AM 1.5) for 3 min while applying a potential of +0.11 V *vs.* RHE (Fig. 6). Although the photoelectrode with a 10 nm-thick  $\text{TiO}_2$  layer underwent a rapid decay, the other photoelectrodes showed stable photocurrents. The highest photocurrent value was observed for a thickness of 30 nm, and the photocurrents decreased with increases in the  $\text{TiO}_2$  thickness.

To investigate the effect of the  $\text{TiO}_2$  thickness in more detail, incident photon to current conversion efficiency (IPCE) spectra were obtained by irradiation with monochromatic light using band pass filters. Fig. 7 shows the IPCE spectra acquired from Pt/ $\text{TiO}_2$ / $\text{Cr}_2\text{O}_3$  specimens with various  $\text{TiO}_2$  layer thicknesses. The IPCE spectra of the electrodes with more than 30 nm thick  $\text{TiO}_2$  layers increased in intensity at 400 nm, showing a good correlation with the absorption spectrum of  $\text{Cr}_2\text{O}_3$  (Fig. 4, blue line). Although the IPCE values at wave-

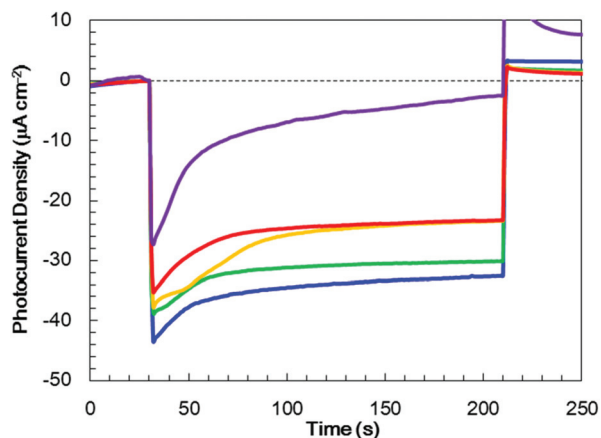


**Fig. 6** Photocurrent transients for Pt/ $\text{TiO}_2$ / $\text{Cr}_2\text{O}_3$  specimens with various  $\text{TiO}_2$  layer thicknesses (10 nm; purple line, 30 nm; blue line, 60 nm; green line, 80 nm; yellow line and 120 nm; red line) at +0.11 V *vs.* RHE in a 0.5 M  $\text{Na}_2\text{CO}_3$ : $\text{NaHCO}_3$  (1:1) buffer electrolyte (pH 9.7) under one sun ( $100 \text{ mW cm}^{-2}$ , AM 1.5) illumination. The thickness of the  $\text{Cr}_2\text{O}_3$  layer was fixed at 60 nm.

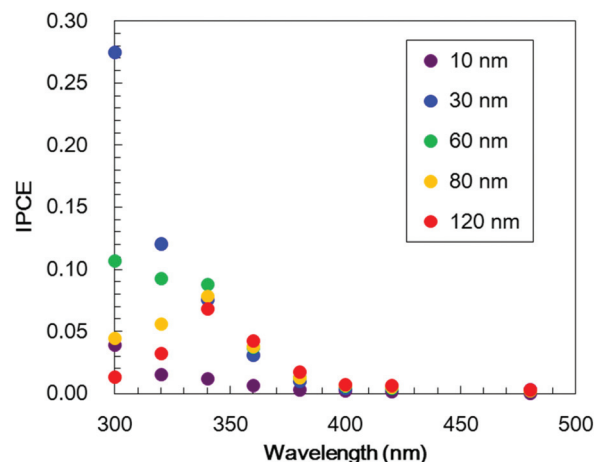


**Fig. 7** IPCE spectra obtained from Pt/ $\text{TiO}_2$ / $\text{Cr}_2\text{O}_3$  electrodes at various wavelengths using different  $\text{TiO}_2$  layer thicknesses (10 nm; purple, 30 nm; blue, 60 nm; green, 80 nm; yellow and 120 nm; red) at +0.11 V *vs.* RHE in a 0.5 M  $\text{Na}_2\text{CO}_3$ : $\text{NaHCO}_3$  (1:1) buffer electrolyte (pH 9.7) under monochromatic illumination. The thickness of the  $\text{Cr}_2\text{O}_3$  layer was fixed at 60 nm.

lengths longer than 340 nm were similar for each electrode, the IPCE values below this point became smaller as the  $\text{TiO}_2$  layer thickness exceeded 30 nm. These results suggest that light absorption by  $\text{Cr}_2\text{O}_3$  was inhibited by the  $\text{TiO}_2$  overlayer. As an example, as shown by the black line in the absorption spectrum in Fig. 4, a  $\text{TiO}_2$  layer having a thickness of 60 nm had an absorbance greater than 1 below 320 nm. Thus, more than 90% of the light below this wavelength could not reach  $\text{Cr}_2\text{O}_3$ . The observation that the IPCE spectra were affected by the  $\text{TiO}_2$  thickness clearly indicates that the cathodic photocurrent originated from the photoexcitation of  $\text{Cr}_2\text{O}_3$ , and that light absorption by  $\text{TiO}_2$  decreased the photocurrent. However, the IPCE values for the photoelectrode with a 10 nm-thick  $\text{TiO}_2$  layer were lower than those of the other electrodes at almost all wavelengths. Although a 10 nm-thick  $\text{TiO}_2$  layer covered the surface of  $\text{Cr}_2\text{O}_3$  (Fig. S5†), the thickness of  $\text{TiO}_2$  may be insufficient for the formation of a p-n junction structure. As a result of the trade-off between the light filtering effect of  $\text{TiO}_2$  and the formation of a charge separation structure, the optimal  $\text{TiO}_2$  film thickness with regard to generating a large photocurrent is believed to be 30 nm.

### PEC water splitting

To confirm PEC  $\text{H}_2$  evolution, the gaseous products were analysed by gas chromatography after 1 h of irradiation with AM 1.5 light while applying a bias of +0.11 V *vs.* RHE (Table 1). The Pt/ $\text{TiO}_2$ (60 nm)/ $\text{Cr}_2\text{O}_3$  specimen generated a stable photocurrent over this time span (Fig. S6†), with a charge flow of  $110 \text{ mC cm}^{-2}$ . During this trial,  $510 \text{ nmol cm}^{-2}$  of  $\text{H}_2$  was produced (entry 1 in Table 1), equivalent to 89% faradaic efficiency. Control experiments without Pt or without both Pt and  $\text{TiO}_2$  did not produce  $\text{H}_2$  (entries 2 and 4, Table 1), while a test without  $\text{TiO}_2$  gave only a very small amount of this product (entry 3 in Table 1). Thus, even if light is absorbed by  $\text{Cr}_2\text{O}_3$ ,



**Table 1** The amounts of charge and H<sub>2</sub> obtained from a 1 h PEC reaction<sup>a</sup>

Entry	Photoelectrode	Charge mC cm <sup>-2</sup>	H <sub>2</sub> nmol cm <sup>-2</sup>
1 <sup>b</sup>	Pt/TiO <sub>2</sub> /Cr <sub>2</sub> O <sub>3</sub>	109.8	510
2	Cr <sub>2</sub> O <sub>3</sub>	13.3	nd
3 <sup>b</sup>	TiO <sub>2</sub> /Cr <sub>2</sub> O <sub>3</sub>	1.7	nd
4	Pt/Cr <sub>2</sub> O <sub>3</sub>	10.5	2

<sup>a</sup> AM 1.5 light irradiation with applying bias at +0.11 V vs. RHE. <sup>b</sup> The thickness of TiO<sub>2</sub> layers was 60 nm.

PEC water splitting does not proceed without TiO<sub>2</sub> and Pt. Therefore, it is considered that PEC water splitting progresses due to the generation of photoexcited electrons in Cr<sub>2</sub>O<sub>3</sub> in response to light absorption. These electrons are transferred to the Pt *via* the TiO<sub>2</sub> charge-separation layer.

## Conclusion

The generation of H<sub>2</sub> *via* solar PEC water-splitting by Cr<sub>2</sub>O<sub>3</sub> was successfully realized following surface modification of the oxide. Bare Cr<sub>2</sub>O<sub>3</sub> was found to produce a significant dark current but a minimal photocurrent. The addition of Pt further deteriorated the performance of this material. Therefore, neither bare Cr<sub>2</sub>O<sub>3</sub> nor Pt/Cr<sub>2</sub>O<sub>3</sub> provided H<sub>2</sub> by PEC water-splitting. Applying a TiO<sub>2</sub> overlayer with subsequent Pt deposition to fabricate a Pt/TiO<sub>2</sub>/Cr<sub>2</sub>O<sub>3</sub> electrode resulted in an enhanced photocurrent and realized solar PEC H<sub>2</sub> generation. The dark current almost disappeared following this surface treatment, suggesting that TiO<sub>2</sub> passivated the Cr<sub>2</sub>O<sub>3</sub> surface. In this layered electrode, a photocathode current was induced in response to light absorption by Cr<sub>2</sub>O<sub>3</sub>, while the TiO<sub>2</sub> layer acted as a filter to inhibit this light absorption. Nevertheless, since the photocurrent was enhanced by the presence of a TiO<sub>2</sub> coating, it is evident that TiO<sub>2</sub> also acted as a charge separation layer. Thus, within the Pt/TiO<sub>2</sub>/Cr<sub>2</sub>O<sub>3</sub> electrode, TiO<sub>2</sub> accumulated photoexcited electrons generated by light absorption by Cr<sub>2</sub>O<sub>3</sub> while blocking undesired interactions between Cr<sub>2</sub>O<sub>3</sub> and Pt. As a result, H<sub>2</sub> generation was realized through water-splitting. In future, the use of this TiO<sub>2</sub> layering technique with a doped Cr<sub>2</sub>O<sub>3</sub> could lead to practical visible-light-driven PEC water-splitting systems.

## Experimental section

### Materials

Tin(IV) oxide/ITO double-layered TCO coated glass (Geomatec Co., Ltd) was used as substrates for the preparation of the electrodes. Commercially available Cr, TiO<sub>2</sub> and Pt sputtering targets and TiO<sub>2</sub> powder were obtained from the Kojundo Chemical Laboratory Co. A reference sample of Cr<sub>2</sub>O<sub>3</sub> for the XPS analysis and UV/Visible diffuse reflectance spectroscopy was obtained from Nacalai Tesque, Inc.

### Preparation

A Cr<sub>2</sub>O<sub>3</sub> film was deposited by RF reactive magnetron sputtering of a Cr target with an Ar/O<sub>2</sub> (9 : 1 v/v) plasma. After deposition, the electrodes were annealed at 823 K under an N<sub>2</sub>/O<sub>2</sub> (4 : 1 v/v) gas flow for 2 h. Subsequently, a TiO<sub>2</sub> layer was deposited on the surface of the Cr<sub>2</sub>O<sub>3</sub> thin film by RF reactive magnetron sputtering of a TiO<sub>2</sub> target with an Ar/O<sub>2</sub> (4 : 1 v/v) plasma. The deposited electrodes were then annealed at 823 K under an O<sub>2</sub> gas flow for 2 h. The Pt cocatalyst was loaded onto either TiO<sub>2</sub>-coated or bare Cr<sub>2</sub>O<sub>3</sub> specimens by RF magnetron sputtering. The amount of Pt applied was adjusted to obtain an average thickness of 1 nm.

### Characterization

The crystal structures of the films were analysed using XRD (Ultima IV, Rigaku Co.) with Cu K $\alpha$  radiation, while the optical properties of the films were assessed by using UV/visible absorption spectroscopy (UV-3600, Shimadzu Co.). STEM together with EDX was performed using a JEM-2100F microscope (JEOL Co.). Samples for these observations were cut using a focused ion beam (FIB; NB5000, Hitachi High-Tech Co.). Prior to cutting the samples, the film surfaces were coated with carbon and Pt layers to protect the specimens from the FIB. XPS data were acquired using a PHI5000 VersaProbe (Ulvac-Phi Co.) spectrometer.

### PEC measurements

The photocurrent density measurements were performed in a three-electrode configuration consisting of a silver–silver chloride (Ag/AgCl) electrode, a platinum wire electrode and a prepared photocathode as the working, reference and counter electrodes, respectively. In these trials, the exposed TCO layer of the photocathode was covered with silicone rubber and all potentials were converted to the RHE reference scale using the equation  $E$  (vs. RHE) =  $E$  (vs. Ag/AgCl) + 0.20 V + 0.059 V  $\times$  pH. A sealed Pyrex® glass cell was employed as the reactor and Ar-saturated aqueous 0.5 M NaHCO<sub>3</sub> : Na<sub>2</sub>CO<sub>3</sub> (1 : 1; pH 9.7) solutions were employed as the electrolytes. An electrochemical analyser (ALS612E and ALSCHI-614C, ALS Co., Ltd) supplied the potential and frequency to the electrode. The electrode was irradiated with a light intensity equivalent to one sun (AM 1.5; 100 mW cm<sup>-2</sup>) using a solar simulator (HAL-320, Asahi Spectra Co.). Prior to exposure, the light intensity was adjusted with a CS-20 instrument (Asahi Spectra Co.). The sample irradiation was limited to an area of 10  $\times$  10 mm *via* a slit. Linear sweep voltammetry was conducted at a scan rate of 50 mV s<sup>-1</sup> under chopped light irradiation. The photocurrent densities in the photocurrent transient curves were converted by subtracting the dark current density values determined just prior to photo-irradiation from the current densities. The PEC water-splitting reaction, in conjunction with the application of an electrical bias, was conducted while measuring the photocurrent generated under continuous irradiation at a fixed electrode potential of -0.5 V vs. Ag/AgCl. After incubation for 30 min to allow the gaseous reaction products to equilibrate





between the liquid and gas phases, these products were analysed by gas chromatography (GC-2014, Shimadzu Co.), employing a thermal conductivity detector and an active carbon column (Shincarbon ST, Shinwa Chemical Industries Co.) with Ar as the carrier gas. IPCE spectra were acquired under monochromatic light generated by a 300 W xenon lamp (MAX-303, Asahi Spectra Co.), using band-pass filters to obtain specific wavelengths.

## Conflicts of interest

There are no conflicts to declare.

## Acknowledgements

The authors wish to thank Ms. Hiroko Uchiyama for technical support.

## Notes and references

- G. Glensk and S. Reichelstein, *Nat. Energy*, 2019, **4**, 216–222.
- D. Parra, L. Valverde, F. J. Pino and M. K. Patel, *Renewable Sustainable Energy Rev.*, 2019, **101**, 279–294.
- I. Staffell, D. Scamman, A. V. Abad, P. Balcombe, P. E. Dodds, P. Ekins, N. Shah and K. R. Ward, *Energy Environ. Sci.*, 2019, **12**, 463–491.
- T. Yao, X. An, H. Han, J. Q. Chen and C. Li, *Adv. Energy Mater.*, 2018, **8**, 1800210.
- C. Jiang, S. J. A. Moniz, A. Wang, T. Zhang and J. Tang, *Chem. Soc. Rev.*, 2017, **46**, 4645–4660.
- J. W. Ager, M. R. Shaner, K. A. Walczak, I. D. Sharp and S. Ardo, *Energy Environ. Sci.*, 2015, **8**, 2811–2824.
- A. Fujishima and K. Honda, *Nature*, 1972, **238**, 37–38.
- A. Kudo and Y. Miseki, *Chem. Soc. Rev.*, 2009, **38**, 253–278.
- R. Abe, *J. Photochem. Photobiol., C*, 2010, **11**, 179–209.
- X. B. Chen, S. H. Shen, L. J. Guo and S. S. Mao, *Chem. Rev.*, 2010, **110**, 6503–6570.
- K. Maeda and K. Domen, *J. Phys. Chem. Lett.*, 2010, **1**, 2655–2661.
- K. Maeda, *J. Photochem. Photobiol., C*, 2011, **12**, 237–268.
- F. E. Osterloh, *Chem. Soc. Rev.*, 2013, **42**, 2294–2320.
- T. Hisatomi, J. Kubota and K. Domen, *Chem. Soc. Rev.*, 2014, **43**, 7520–7535.
- A. Miyoshi, S. Nishioka and K. Maeda, *Chem. – Eur. J.*, 2018, **24**, 18204–18219.
- Y. Miseki and K. Sayama, *Adv. Energy Mater.*, 2019, **9**, 1801294.
- T. Morikawa, S. Sato, K. Sekizawa, T. Arai and T. M. Suzuki, *ChemSusChem*, 2019, **12**, 1807–1824.
- H. Yoneyama, H. Sakamoto and H. Tamura, *Electrochim. Acta*, 1975, **20**, 341–345.
- K. Ohashi, J. McCann and J. O. M. Bockris, *Nature*, 1977, **266**, 610–611.
- J. E. Turner, M. Hendewerk, J. Parmeter, D. Neiman and G. A. Somorjai, *J. Electrochem. Soc.*, 1984, **131**, 1777–1783.
- M. S. Prévot and K. Sivula, *J. Phys. Chem. C*, 2013, **117**, 17879–17893.
- K. Zhang, M. Ma, P. Li, D. H. Wang and J. H. Park, *Adv. Energy Mater.*, 2016, **6**, 1600602.
- A. Liu, H. Zhu and Y.-Y. Noh, *Mater. Sci. Eng., R*, 2019, **135**, 85–100.
- Z. Wang, P. K. Nayak, J. A. Caraveo-Frescas and H. N. Alshareef, *Adv. Mater.*, 2016, **28**, 3831–3892.
- A. Paracchino, V. Laporte, K. Sivula, M. Gratzel and E. Thimsen, *Nat. Mater.*, 2011, **10**, 456–461.
- S. N. F. M. Nasir, M. K. N. Yahya, N. W. M. Sopian, N. A. Ludin, M. A. Ibrahim, K. Sopian and M. A. M. Teridi, *RSC Adv.*, 2016, **6**, 56885–56891.
- S. Ida, K. Yamada, T. Matsunaga, H. Hagiwara, Y. Matsumoto and T. Ishihara, *J. Am. Chem. Soc.*, 2010, **132**, 17343–17345.
- K. Sekizawa, T. Nonaka, T. Arai and T. Morikawa, *ACS Appl. Mater. Interfaces*, 2014, **6**, 10969–10973.
- T. Morikawa, T. Arai and T. Motohiro, *Appl. Phys. Express*, 2013, **6**, 041201.
- A. Holt and P. Kofstad, *Solid State Ionics*, 1997, **100**, 201–209.
- H. Cao, X. Qiu, Y. Liang, M. Zhao and Q. Zhu, *Appl. Phys. Lett.*, 2006, **88**, 241112.
- L. W. Finger and R. M. Hazen, *J. Appl. Phys.*, 1980, **51**, 5362–5367.
- L. Pauling and S. B. Hendricks, *J. Am. Chem. Soc.*, 1925, **47**, 781–790.
- A. Holt and P. Kofstad, *Solid State Ionics*, 1999, **117**, 21–25.
- S. C. Tsai, A. M. Huntz and C. Dolin, *Mater. Sci. Eng., A*, 1996, **212**, 6–13.
- A. Holt and P. Kofstad, *Solid State Ionics*, 1994, **69**, 127–136.
- B. Medasani, M. L. Sushko, K. M. Rosso, D. K. Schreiber and S. M. Bruemmer, *J. Phys. Chem. C*, 2018, **122**, 12984–12993.
- F. Lebreau, M. M. Islam, B. Diawara and P. Marcus, *J. Phys. Chem. C*, 2014, **118**, 18133–18145.
- K. Sekizawa, K. Oh-ishi, K. Kataoka, T. Arai, T. M. Suzuki and T. Morikawa, *J. Mater. Chem. A*, 2017, **5**, 6483–6493.
- M. T. Greiner, M. G. Helander, W.-M. Tang, Z.-B. Wang, J. Qiu and Z.-H. Lu, *Nat. Mater.*, 2012, **11**, 76–81.
- Y. Xu and M. A. A. Schoonen, *Am. Mineral.*, 2000, **85**, 543–556.
- L. Farrell, K. Fleischer, D. Caffrey, D. Mullarkey, E. Norton and I. V. Shvets, *Phys. Rev. B: Condens. Matter Mater. Phys.*, 2015, **91**, 125202.
- E. Arca, K. Fleischer and I. V. Shvets, *Appl. Phys. Lett.*, 2011, **99**, 111910.
- H. Wang, Y. Zhang, L. Zhang, Y. Guo, S. Liu, F. Gao, Y. Han, G. Feng, X. Liang and L. Ge, *RSC Adv.*, 2016, **6**, 84871–84881.
- S. Goel, A. Kumar, J. K. Quamara and J. Kumar, *Adv. Sci. Lett.*, 2014, **20**, 1562–1566.
- J. J. Carey, M. Legesse and M. Nolan, *J. Phys. Chem. C*, 2016, **120**, 19160–19174.



- 47 E. Arca, K. Fleischer, S. A. Krasnikov and I. Shvets, *J. Phys. Chem. C*, 2013, **117**, 21901–21907.
- 48 D. Bae, B. Seger, P. C. K. Vesborg, O. Hansen and I. Chorkendorff, *Chem. Soc. Rev.*, 2017, **46**, 1933–1954.
- 49 N. Guijarro, M. S. Prevot and K. Sivula, *Phys. Chem. Chem. Phys.*, 2015, **17**, 15655–15674.
- 50 B. Xu, L. Tian, A. S. Etman, J. Sun and H. Tian, *Nano Energy*, 2019, **55**, 59–64.
- 51 M. C. Biesinger, B. P. Payne, A. P. Grosvenor, L. W. M. Lau, A. R. Gerson and R. S. C. Smart, *Appl. Surf. Sci.*, 2011, **257**, 2717–2730.
- 52 R. Cheng, B. Xu, C. N. Borca, A. Sokolov, C.-S. Yang, L. Yuan, S.-H. Liou, B. Doudin and P. A. Dowben, *Appl. Phys. Lett.*, 2001, **79**, 3122–3124.
- 53 M. M. Abdullah, F. M. Rajab and S. M. Al-Abbas, *AIP Adv.*, 2014, **4**, 027121.
- 54 C.-S. Cheng, H. Gomi and H. Sakata, *Phys. Status Solidi A*, 1996, **155**, 417–425.
- 55 R. Cohen, L. Kronik, A. Shanzer, D. Cahen, A. Liu, Y. Rosenwaks, J. K. Lorenz and A. B. Ellis, *J. Am. Chem. Soc.*, 1999, **121**, 10545–10553.
- 56 Y. Li, L. Zhang, W. Wu, P. Dai, X. Yu, M. Wu and G. Li, *Nanoscale Res. Lett.*, 2014, **9**, 270.

